


Nucleocapsid protein of SARS-CoV-2 phase separates into RNA-rich polymerase-containing condensates

Adriana Savastano^{1,3}, Alain Ibáñez de Opakua^{1,3}, Marija Rankovic^{2,3} & Markus Zweckstetter^{1,2}  [✉]

The etiologic agent of the Covid-19 pandemic is the severe acute respiratory syndrome coronavirus 2 (SARS-CoV-2). The viral membrane of SARS-CoV-2 surrounds a helical nucleocapsid in which the viral genome is encapsulated by the nucleocapsid protein. The nucleocapsid protein of SARS-CoV-2 is produced at high levels within infected cells, enhances the efficiency of viral RNA transcription, and is essential for viral replication. Here, we show that RNA induces cooperative liquid-liquid phase separation of the SARS-CoV-2 nucleocapsid protein. In agreement with its ability to phase separate *in vitro*, we show that the protein associates in cells with stress granules, cytoplasmic RNA/protein granules that form through liquid-liquid phase separation and are modulated by viruses to maximize replication efficiency. Liquid-liquid phase separation generates high-density protein/RNA condensates that recruit the RNA-dependent RNA polymerase complex of SARS-CoV-2 providing a mechanism for efficient transcription of viral RNA. Inhibition of RNA-induced phase separation of the nucleocapsid protein by small molecules or biologics thus can interfere with a key step in the SARS-CoV-2 replication cycle.

¹German Center for Neurodegenerative Diseases (DZNE), Von-Siebold-Str. 3a, 37075 Göttingen, Germany. ²Department for NMR-based Structural Biology, Max Planck Institute for Biophysical Chemistry, Am Faßberg 11, 37077 Göttingen, Germany. ³These authors contributed equally: Adriana Savastano, Alain Ibáñez de Opakua, Marija Rankovic. ✉email: Markus.Zweckstetter@dzne.de

The etiologic agent of the Covid-19 pandemic is the severe acute respiratory syndrome coronavirus 2 (SARS-CoV-2) (<https://www.who.int/emergencies/diseases/novel-coronavirus-2019>). SARS-CoV-2 is an enveloped single-stranded, positive-sense RNA virus with a 30 kb genome, one of the largest among RNA viruses^{1,2}. The viral membrane of SARS-CoV-2, which contains the spike protein, a glycoprotein, and the envelope protein^{1,3}, surrounds a helical nucleocapsid. In the nucleocapsid, the viral genome is encapsulated by the nucleocapsid protein and thereby protected from the host cell environment^{4,5}. The nucleocapsid protein of human coronaviruses is produced at high levels within infected cells and is critical for virion assembly⁴⁻⁷. In addition, it enhances the efficiency of sub-genomic viral RNA transcription and is essential for viral replication⁴. Because of its importance for diagnostic and therapeutic approaches to treat Covid-19^{8,9}, there is an urgent need to define the molecular mechanisms that underlie the nucleocapsid protein's fundamental viral role.

Liquid-liquid phase separation (LLPS) provides a highly cooperative mechanism to locally concentrate proteins and nucleic acids and promote cellular reactions^{10,11}. Recent evidence indicates that negative-sense RNA viruses, which replicate in the cytoplasm of infected cells¹², concentrate their replication machinery in dynamic compartments formed by LLPS of the viral structural proteins L, phosphoprotein (P), and nucleocapsid (N) protein^{13,14}. The genomes of positive-sense RNA viruses such as SARS-CoV-2, however, lack the genetic code for the phosphoprotein P, which is essential for LLPS in negative-sense RNA viruses¹³⁻¹⁵.

Here we investigate liquid-liquid phase separation of the nucleocapsid protein of SARS-CoV-2 and show that nucleocapsid protein LLPS concentrates components of the SARS-CoV-2 replication machinery providing a mechanism for enhanced viral transcription and replication.

Results

LLPS of N^{SARS-CoV-2} and RNA into protein/RNA-dense compartments. To investigate if the N protein of SARS-CoV-2 (further termed N^{SARS-CoV-2}; Fig. 1a) phase separates in the absence of other viral proteins, we measured the turbidity of N^{SARS-CoV-2} solutions at different protein concentrations. Up to 50 μ M, the protein solution retained low absorbance (Fig. 1b), despite its tendency to oligomerize¹⁶. Next, we tested LLPS of N^{SARS-CoV-2} in the presence of RNA. The 419-residue N^{SARS-CoV-2} contains an RNA-binding domain and a C-terminal dimerization domain embedded into long intrinsically disordered regions (Fig. 1a)^{4,5}. The globular domains as well as the intrinsically disordered regions of coronavirus N proteins bind to RNA⁴. At 50 μ M protein concentration, the addition of 1 μ M polyU (800 kDa), which we used as a substitute for viral RNA, strongly increased turbidity (Fig. 1b). Differential interference contrast (DIC) and fluorescent microscopy demonstrated the formation of spherical droplets (Fig. 1c). The droplets contained both N^{SARS-CoV-2} and RNA (Fig. 1c). N^{SARS-CoV-2}/polyU droplets were robust against the presence of the aliphatic alcohol 1,6-hexanediol (Supplementary Fig. 1a). In contrast, the addition of increasing amounts of NaCl dissolved the droplets (Supplementary Fig. 1b), indicating an important role of electrostatic interactions for RNA-induced LLPS of N^{SARS-CoV-2}. Quantification of fluorescence intensities of N^{SARS-CoV-2} and RNA showed that their concentration is strongly increased inside droplets (Fig. 1d), i.e., cooperative LLPS of N^{SARS-CoV-2} and RNA into protein/RNA-dense compartments occurs.

Next, we monitored LLPS for different N^{SARS-CoV-2} and polyU concentrations. According to turbidity measurements, polyU-

induced LLPS started at 5–10 μ M N^{SARS-CoV-2} (Fig. 1b and Supplementary Fig. 1c). The polyU concentration at which maximum turbidity was observed shifted to higher polyU concentrations with increasing protein concentration (Fig. 1b and Supplementary Fig. 1c). Calculation of the N^{SARS-CoV-2} and polyU charge showed that LLPS is strongest when charge neutralization occurs (Fig. 1b). At a given protein concentration, the turbidity increased with increasing polyU concentration, reached a maximum, and then rapidly decreased to its starting value (Fig. 1b), i.e., charge-matching RNA concentrations enable phase separation, but high RNA/protein ratios prevent LLPS of N^{SARS-CoV-2}. The RNA-induced LLPS behavior of N^{SARS-CoV-2} is in agreement with the known properties of RNA-induced phase separation of prion-like RNA binding proteins¹⁷.

Time-dependent transformation of N^{SARS-CoV-2}/RNA-droplets. A characteristic property of LLPS is the liquid-like nature of phase-separated compartments. We photobleached N^{SARS-CoV-2} inside of N^{SARS-CoV-2}/polyU droplets and observed rapid recovery of fluorescence (Fig. 1e). We then waited one hour and repeated fluorescence recovery after photobleaching (FRAP). At this later time point, the fluorescence recovery was best described by a bi-exponential fit consisting of two components (Fig. 1e and Supplementary Fig. 1d). In addition, the fluorescence did not fully recover (Fig. 1e), i.e., ~60% of N^{SARS-CoV-2} had transformed into an immobile species. The analysis shows that N^{SARS-CoV-2}/polyU droplets change their material properties in a time-dependent manner. Because a major activity of N^{SARS-CoV-2} is to encapsulate RNA, the immobile fraction observed by FRAP might represent the early stages of nucleocapsid assembly. Successful nucleocapsid formation, however, also depends on the specific sequence and secondary structure of viral RNA¹⁸ and is therefore not expected for polyU.

SARS-CoV-2 nucleocapsid protein associates with stress granules. Stress granules (SGs) are cytoplasmic RNA/protein granules, which form through LLPS and are modulated by coronavirus and other viruses to maximize replication efficiency^{19,20}. SARS-CoV-2 protein interaction mapping indicated that N^{SARS-CoV-2} binds the SG protein G3BP1²¹. To investigate if N^{SARS-CoV-2} associates with SGs, we used a previously established SG-colocalization assay²². SGs were induced in HeLa cells by arsenite followed by permeabilization of the plasma membrane by digitonin. Subsequently, soluble cytosolic factors were washed out and fluorescently labeled N^{SARS-CoV-2} was added together with Alexa Fluor 594-coupled antibody against the SG marker G3BP1. Laser scanning confocal microscopy showed arsenite-induced formation of SGs that stained for G3BP1 (Fig. 2a). N^{SARS-CoV-2} colocalized with G3BP1-positive SGs (Fig. 2a; Supplementary Movie 1). FRAP of SG-associated N^{SARS-CoV-2} suggested the presence of three N^{SARS-CoV-2} populations (Fig. 2b): a very mobile with rapid fluorescence recovery, a slower diffusing component, and an immobile fraction, which does not recover its fluorescence after photobleaching (Fig. 2c). Because SGs consists of a rigid core and a dynamic shell²³, we attribute the different N^{SARS-CoV-2} diffusion properties to the localization of N^{SARS-CoV-2} to different sub-structures of SGs. In agreement with our findings for N^{SARS-CoV-2}, the N protein of SARS-CoV, the causative agent of the SARS epidemic in 2002/2003, translocates to SGs in stressed SARS-CoV-infected cells²⁴.

RNA-interaction of the mutation-prone SR-region. RNA viruses have enormously high mutation rates enhancing virulence and evolvability. On June 7th 2020, already 42176 SARS-CoV-2 sequences were deposited (<https://www.gisaid.org>). Analysis of

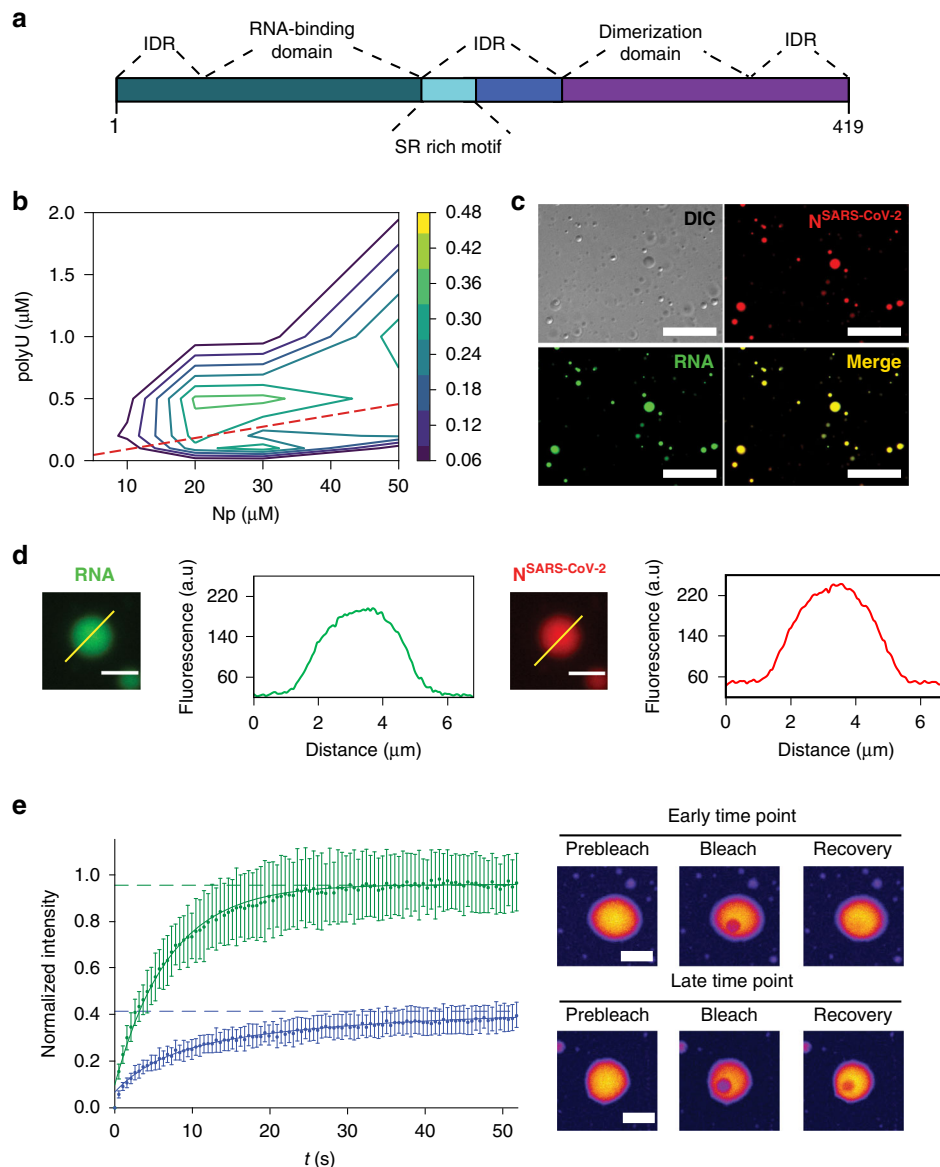


Fig. 1 RNA-induced LLPS of the nucleocapsid protein of SARS-CoV-2. **a** Organization of N^{SARS-CoV-2} into two globular domains (RNA-binding domain and C-terminal dimerization domain) surrounded by long intrinsically disordered regions (IDR)^{4,5}. The serine/arginine (SR)-rich region is conserved in coronaviruses. **b** Influence of RNA and protein concentration on N^{SARS-CoV-2}/polyU-LLPS in 20 mM NaPi, pH 7.5, monitored by solution turbidity at 350 nm. Average values from three independent measurements are shown. The dashed line marks N^{SARS-CoV-2}/polyU-concentrations at which charge neutralization occurs, assuming a charge of -1 per phosphate group. **c** Fluorescence and DIC microscopy of spherical droplets of 50 μ M N^{SARS-CoV-2} and 1 μ M polyU in 20 mM NaPi, pH 7.5. Fluorescently labeled RNA (green) partitioned into the droplets. Scale bar, 20 μ m. Micrographs are representative of three independent biological replicates. **d** Increase in N^{SARS-CoV-2}- and RNA-concentration inside of N^{SARS-CoV-2}/polyU droplets in 20 mM NaPi, pH 7.5. Scale bars 3 μ m. Micrographs are representative of three independent biological replicates. **e** Time-dependent change in diffusion of N^{SARS-CoV-2} inside polyU-induced droplets observed by FRAP. FRAP of freshly prepared droplets is shown in green, and after incubation for one hour in blue. Error bars represent the standard deviation for averaged six curves for each time point. Representative micrographs of a fresh droplet (top) and after incubation for one hour (bottom) before bleaching, after bleaching, and at the end of recovery are displayed to the right. Scale bars 10 μ m.

the corresponding N proteins showed that the mutations are most frequent in the SR-region of N^{SARS-CoV-2} (Fig. 3a), which is conserved among human coronaviruses (Supplementary Fig. 2). SR-regions bind both RNA and proteins²⁵. To gain insight into the molecular properties of the SR-region of N^{SARS-CoV-2} and its interaction with RNA, we combined NMR spectroscopy with molecular dynamics (MD) simulations. We particularly focused on the region from A182 to S197, because it contains 9 serine and 4 arginine residues, i.e., the highest density of SR-motifs in N^{SARS-CoV-2} (Supplementary Fig. 2). Chemical shift analysis

showed that residues A182-S197 are very dynamic with a small propensity of α -helical structure next to R189 (Fig. 3b-c).

Next, we investigated the conformational properties of A182-S197 with MD simulations. For the simulations, we used the state-of-the-art force field/water model that accurately reproduced NMR parameters of the intrinsically disordered protein α -synuclein²⁶. In agreement with the NMR analysis, residues next to R189 populate transient α -helical structure (Fig. 3c). We then performed calculations in the presence of polyU. A large number of intermolecular contacts between the arginine residues and the

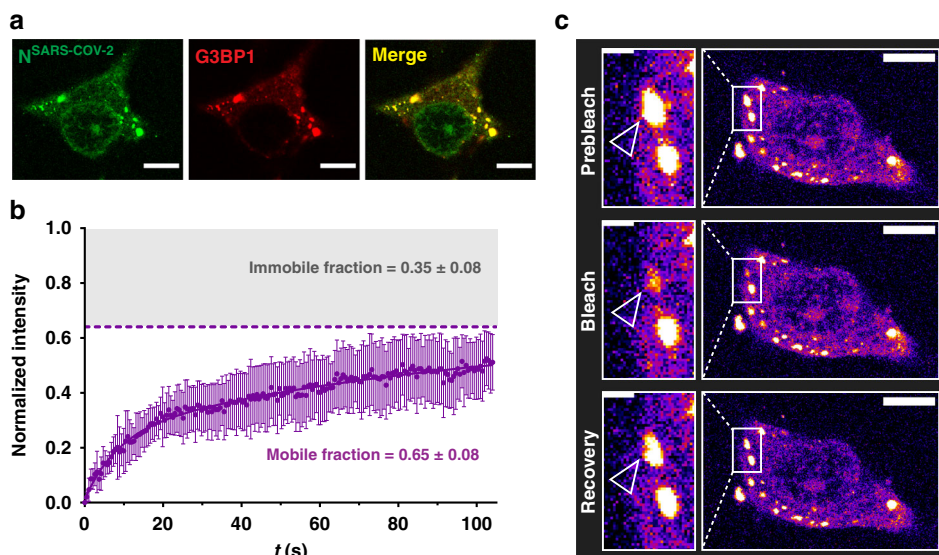


Fig. 2 Nucleocapsid protein of SARS-CoV-2 associates with stress granules. **a** Alexa Fluor 488 labeled N^{SARS-CoV-2} (green) colocalizes with the stress granule marker G3BP1 (red) in arsenite-treated digitonin-permeabilized HeLa cells. Micrographs are representative of three independent biological replicates. **b** Fluorescence recovery after photobleaching (FRAP) curve fitted with bi-exponential fit suggests the existence of a fast diffusing population of molecules, which together with a slowly recovering population comprises ~65% of the bleached spot (mobile fraction). The remaining 35% are immobile and do not recover its fluorescence after photobleaching. The curve is the average of $n = 6$ stress granules, error bars represent standard deviation. **c** Corresponding confocal microscopy pictures of the representative FRAP of N^{SARS-CoV-2} associated with stress granules in HeLa cells. Insert shows the bleached stress granule marked with an arrow. Micrographs are representative of $n = 6$ FRAP experiments in one biological sample. Scale bar 10 μm in **(a)** and **(c)**, 2 μm in the inset in **(c)**.

RNA phosphate groups were observed. Most intermolecular contacts were present for R189 (Fig. 3d, red; Supplementary Fig. 3). In addition, R189 was most sensitive to the addition of polyU as observed by NMR spectroscopy (Fig. 3d, blue; Supplementary Fig. 4a). R189 is the only residue in the region from A182-S197 that is not mutated in 42176 SARS-CoV-2 sequences (Fig. 3d, gray bars), in agreement with its functional relevance.

SR-phosphorylation modulates RNA-induced phase separation. Phosphorylation of SR-domains provides functional specificity and adjustability to ribonucleoprotein formation²⁵ and impairs binding of SR-domains of pre-mRNA splicing factors to protein hydrogel droplets²⁷. To gain insight into the impact of phosphorylation of the SR-region of N^{SARS-CoV-2} on its RNA binding, we performed MD simulations of the high-density SR-stretch carrying phosphate groups at different serine residues (Supplementary Fig. 5a). Even when only a single serine, S188, was phosphorylated, the number of intra- and intermolecular peptide/peptide contacts increased (Supplementary Fig. 5b–c). Multi-site phosphorylation further raised the number of contacts (Supplementary Fig. 5b–c), and the intermolecular peptide/peptide contacts reached a maximum when three serines were phosphorylated (Supplementary Fig. 5c), i.e., when the overall charge is around zero. The phosphorylation-induced increase in intra- and intermolecular contacts is predominantly due to the formation of salt bridges between the phosphate groups and arginine side chains (Supplementary Fig. 5b–c). Because of the dense network of intra- and interpeptide salt bridges, contact formation with RNA—either polyU or a structured RNA derived from the viral genome of SARS-CoV-2—was strongly attenuated upon phosphorylation (Fig. 4a and Supplementary Fig. 6).

To validate the results from MD simulation, we phosphorylated the SR-peptide in vitro using the serine/arginine protein kinase 1 (SRPK1) and performed NMR spectroscopy. SRPK1 phosphorylates SR-motifs and is involved in a wide spectrum of

cellular activities including the regulation of viral genome replication^{25,28}. SRPK1-phosphorylation resulted in two species, a single phosphorylation at S188 (Fig. 4b, middle) and a di-phosphorylated state, which is heterogeneously phosphorylated at four different serines (Fig. 4b, bottom; Supplementary Fig. 7). NMR titrations showed that the unmodified SR-peptide strongly interacts with polyU, but not when it is phosphorylated at S188 (Fig. 4b and Supplementary Fig. 4b). LLPS experiments further demonstrated that phosphorylation of full-length N^{SARS-CoV-2} by SRPK1 changes its RNA-induced phase separation behavior (Fig. 4c and Supplementary Fig. 8). The maximum of RNA-induced turbidity was shifted to lower polyU-concentrations for SRPK1-phosphorylated N^{SARS-CoV-2} (Fig. 4c). In addition, fluorescently labeled RNA was less recruited to droplets formed by SRPK1-phosphorylated N^{SARS-CoV-2} (Fig. 4d). In agreement with an attenuated interaction of N^{SARS-CoV-2} with RNA upon SRPK1-phosphorylation, we also observed a more rapid diffusion of SRPK1-phosphorylated N^{SARS-CoV-2} inside of polyU-induced droplets when compared to the unmodified protein (Fig. 4e). On the other hand, SRPK1-phosphorylated N^{SARS-CoV-2} still colocalized with stress granules (Fig. 4d).

Nucleocapsid protein LLPS concentrates components of the SARS-CoV-2 replication machinery. LLPS provides a cooperative mechanism to locally increase protein and RNA concentrations^{11,12}. In addition, protein/RNA condensates can recruit additional proteins to promote reactions. To investigate if the catalytic component of RdRp is recruited to N^{SARS-CoV-2}/polyU droplets. Fluorescence microscopy revealed strong nsp12 fluorescence inside the droplets (Fig. 5b). Next, nsp12, nsp7, and nsp8 were reconstituted in a 1:1:2 stoichiometry

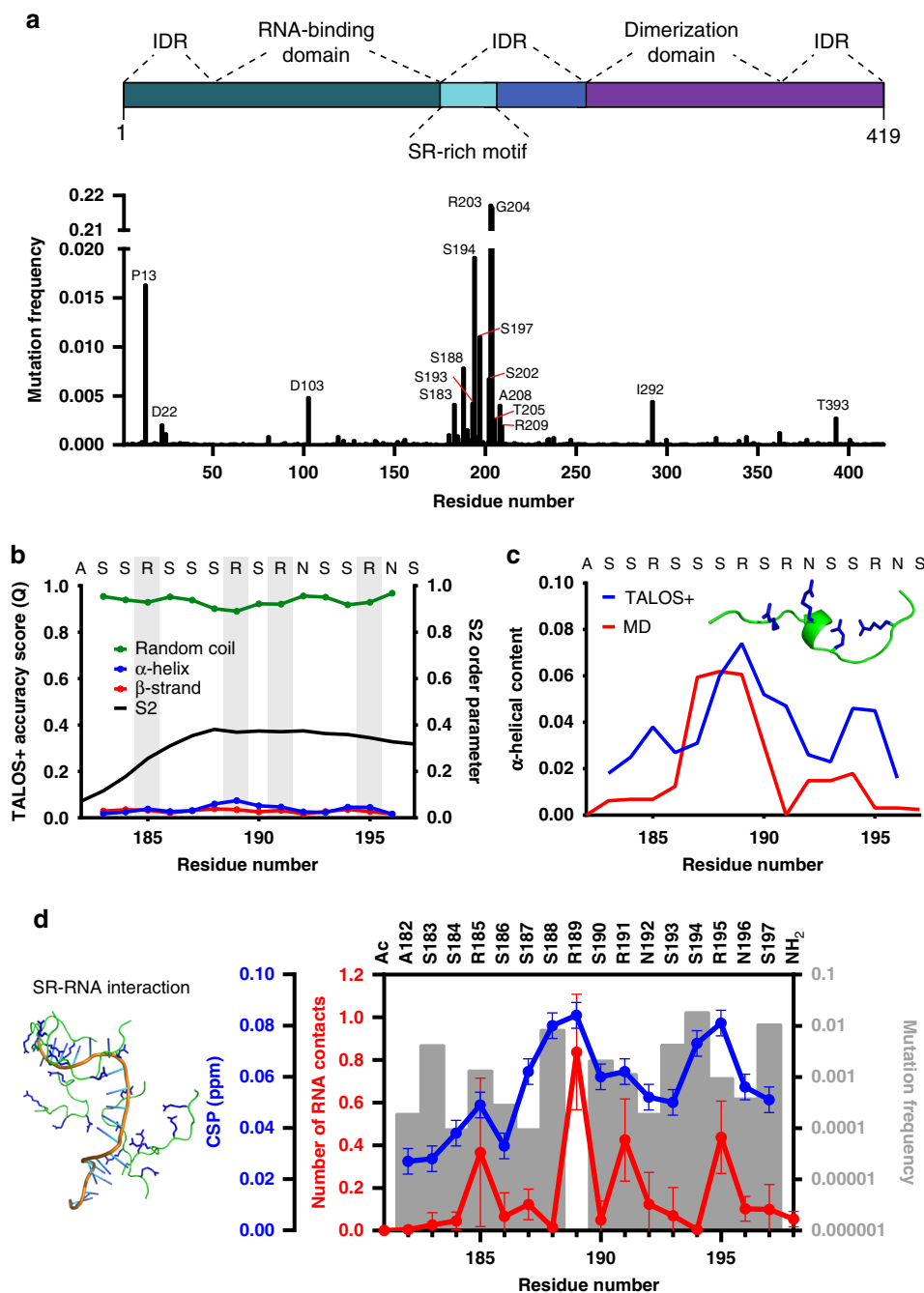


Fig. 3 Atomic details of the RNA-interaction of the mutation-prone SR-region. **a** Frequency of mutations in the nucleocapsid protein in 42176 SARS-CoV-2 sequences from the China National Center for Bioinformatics. Residues with more than 0.0025 frequency are labeled. Domain organization of N^{SARS-CoV-2} on top. **b** NMR-based analysis of the structure of the high-density SR-stretch (residues A182-S197) of N^{SARS-CoV-2}. Secondary structure derived from chemical shifts using TALOS+³⁶ is represented together with the S² order parameter. Arginines are highlighted in gray. **c** Comparison between the α-helical propensity derived from NMR data (blue) and MD simulations (red). One conformer with α-helical content from the simulation is shown inside the graph. **d** Comparison between the number of peptide-polyU contacts per peptide in the MD simulations (red; average and standard deviation of five simulations), the NMR chemical shift perturbation (CSP) of the peptide-polyU titration at 1500 nM of polyU (blue), and the frequency of mutations per residue (gray bars). At the left, a MD snapshot of five SR-peptides with the 20 base length polyU is shown.

together with a RNA template-product duplex, which carried fluorescein at the 5' end²⁹. The RdRp/RNA-complex was added to preformed N^{SARS-CoV-2}/polyU droplets into which the RdRp/RNA-complex was recruited (Fig. 5c). High local concentrations of RdRp and N^{SARS-CoV-2} were reached (Supplementary Fig. 9).

We then investigated the influence of phosphorylation of N^{SARS-CoV-2} by the kinase SRPK1 on the recruitment of nsp12 and the RdRp/RNA-complex into N^{SARS-CoV-2}/RNA droplets.

The analysis showed that both nsp12 and the RdRp/RNA-complex partition less into the droplets formed by SRPK1-phosphorylated N^{SARS-CoV-2} (Fig. 5d). This indicates that N^{SARS-CoV-2} not only interacts with RNA but also directly binds to nsp12 and the nsp12/N^{SARS-CoV-2}-interaction is attenuated by phosphorylation of the SR-region of N^{SARS-CoV-2}. This mechanism was further supported by a more rapid recovery of fluorescence after photobleaching of nsp12 in droplets formed

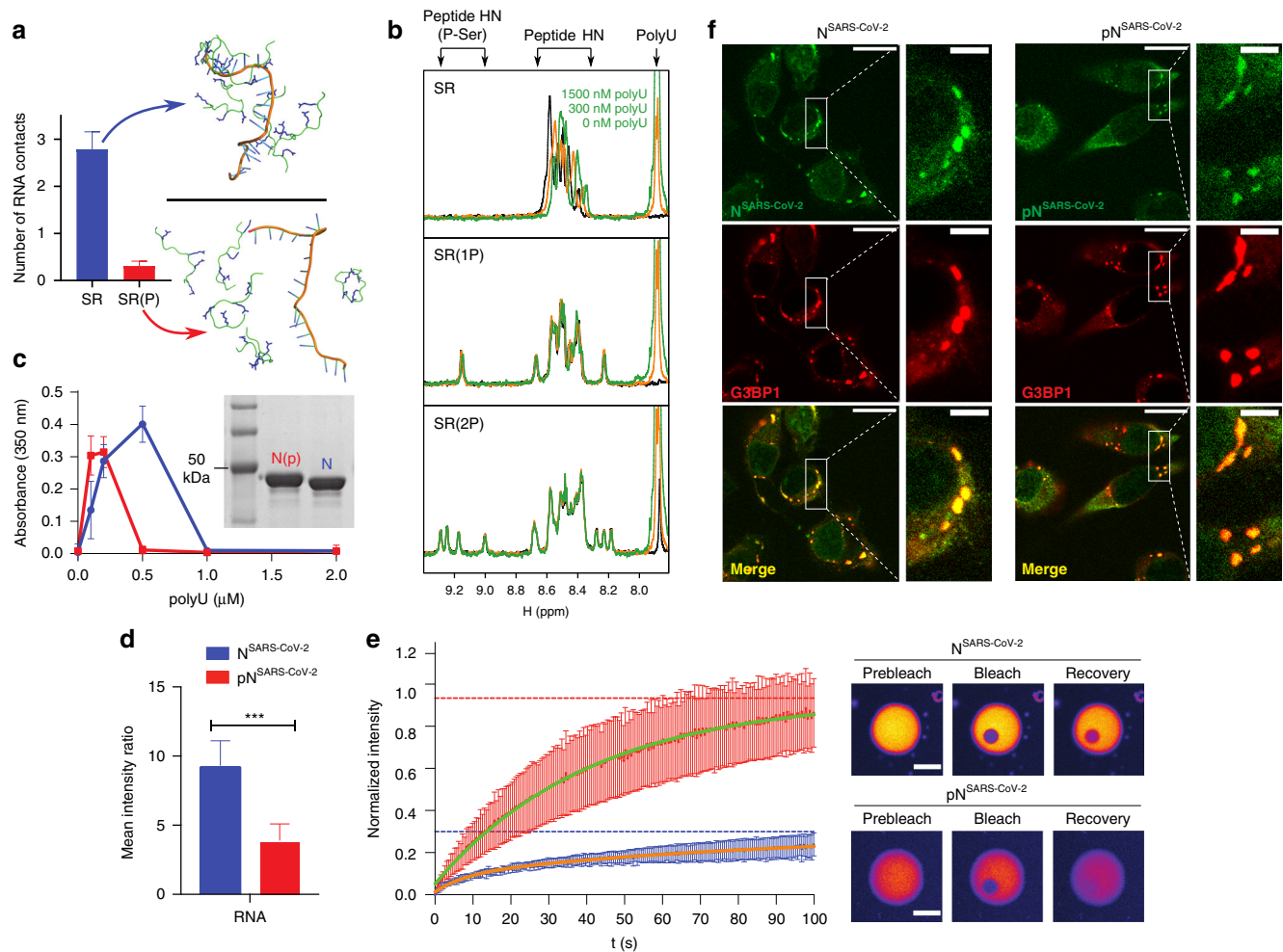


Fig. 4 SR-phosphorylation modulates RNA-induced condensation of the nucleocapsid protein. **a** MD simulations of SR/polyU-interaction. The number of contacts per peptide with a 20 base length polyU is shown in the top graph for the non-phosphorylated and fully phosphorylated SR-peptide as the average and standard deviation of five independent simulations. Snapshots of both peptides are shown. **b** ^1H 1D experiments of the SR-peptide (1766.8 Da), SPRK1 single-phosphorylated peptide (SR(1P); 1846.9 Da according to mass spectrometry; Supplementary Fig. 8) and SPRK1 double-phosphorylated peptide (SR(2P); 1926.9 Da according to mass spectrometry; Supplementary Fig. 8) at three different concentrations of polyU (0, 300 and 1500 nM). The spectral regions, in which the signals of polyU, the backbone H^{N} s of unmodified residues and phosphorylated serines are located, are marked. The positive charges of the SR-peptide are compensated by the polyU negative charges at around 300 nM. **c** Turbidity at 350 nm of solutions of non-phosphorylated (blue) and SRPK1-phosphorylated (red) $\text{N}^{\text{SARS-CoV-2}}$ in 20 mM NaPi, pH 7.5, at 30 μM protein concentration and increasing concentrations of polyU. Average values from three independent measurements are shown. Error bars, std. An SDS-Page gel (insert) displays a band shift due to SRPK1-phosphorylation. **d** Decreased RNA recruitment into polyU-induced droplets of $\text{N}^{\text{SARS-CoV-2}}$ upon phosphorylation with SRPK1 kinase. Mean values and standard deviation are displayed ($n = 100$ droplets). Two-sided t test with P value set to < 0.05 for statistical significance, $*** < 0.001$, $** < 0.002$ and $* < 0.033$, $\text{ns} < 0.12$. **e** FRAP of $\text{N}^{\text{SARS-CoV-2}}$ (blue) and SRPK1-phosphorylated $\text{N}^{\text{SARS-CoV-2}}$ (red) inside of polyU-induced droplets. Error bars represent the standard deviation for averaged 8 and 10 curves for unmodified and phosphorylated $\text{N}^{\text{SARS-CoV-2}}$, respectively. Representative micrographs of $\text{N}^{\text{SARS-CoV-2}}$ (top) and SRPK1-phosphorylated $\text{N}^{\text{SARS-CoV-2}}$ droplets (bottom) before bleaching, after bleaching and at the end of recovery are displayed to the right. Partition coefficients of 12.2 ± 2.8 and 4.3 ± 1.2 were calculated for $\text{N}^{\text{SARS-CoV-2}}$ and phosphorylated $\text{N}^{\text{SARS-CoV-2}}$, respectively. Scale bars, 10 μm . **f** Association of unmodified ($\text{N}^{\text{SARS-CoV-2}}$, left panels) and phosphorylated (phospho $\text{N}^{\text{SARS-CoV-2}}$, right panels) nucleocapsid protein of SARS-CoV-2 with stress granules in HeLa cells, micrographs are representative of two independent biological replicates. Scale bar 20 μm , 5 μm in inset.

by SRPK1-phosphorylated $\text{N}^{\text{SARS-CoV-2}}$ (Fig. 5e). The data suggest that RNA-driven condensation of $\text{N}^{\text{SARS-CoV-2}}$ provides a mechanism for bringing together components of the viral replication machinery (Fig. 5f). In agreement with this proposed mechanism, N protein of SARS-CoV-2 colocalizes intracellularly with replicase components³⁰.

Discussion

Our study shows that the nucleocapsid protein of the SARS-CoV-2 virus undergoes RNA-induced liquid-liquid phase separation. Although nucleocapsid assembly can occur outside of liquid-like

compartments, it was shown that the rate of assembly is increased when the nucleocapsid protein of Measles virus is concentrated through LLPS¹⁵. In addition, $\text{N}^{\text{SARS-CoV-2}}$ interacts with human ribonucleoproteins²¹, which are found in several LLPS-driven cytosolic protein/RNA granules, suggesting that $\text{N}^{\text{SARS-CoV-2}}$ might modulate protein/RNA granule formation in order to maximize viral replication³¹. In agreement with such activity, we showed that $\text{N}^{\text{SARS-CoV-2}}$ translocates to stress granules in stressed cells.

We demonstrate that $\text{N}^{\text{SARS-CoV-2}}$ LLPS promotes cooperative association of the RNA-dependent RNA polymerase complex with polyU RNA in vitro. This suggests that SARS-CoV-2 uses

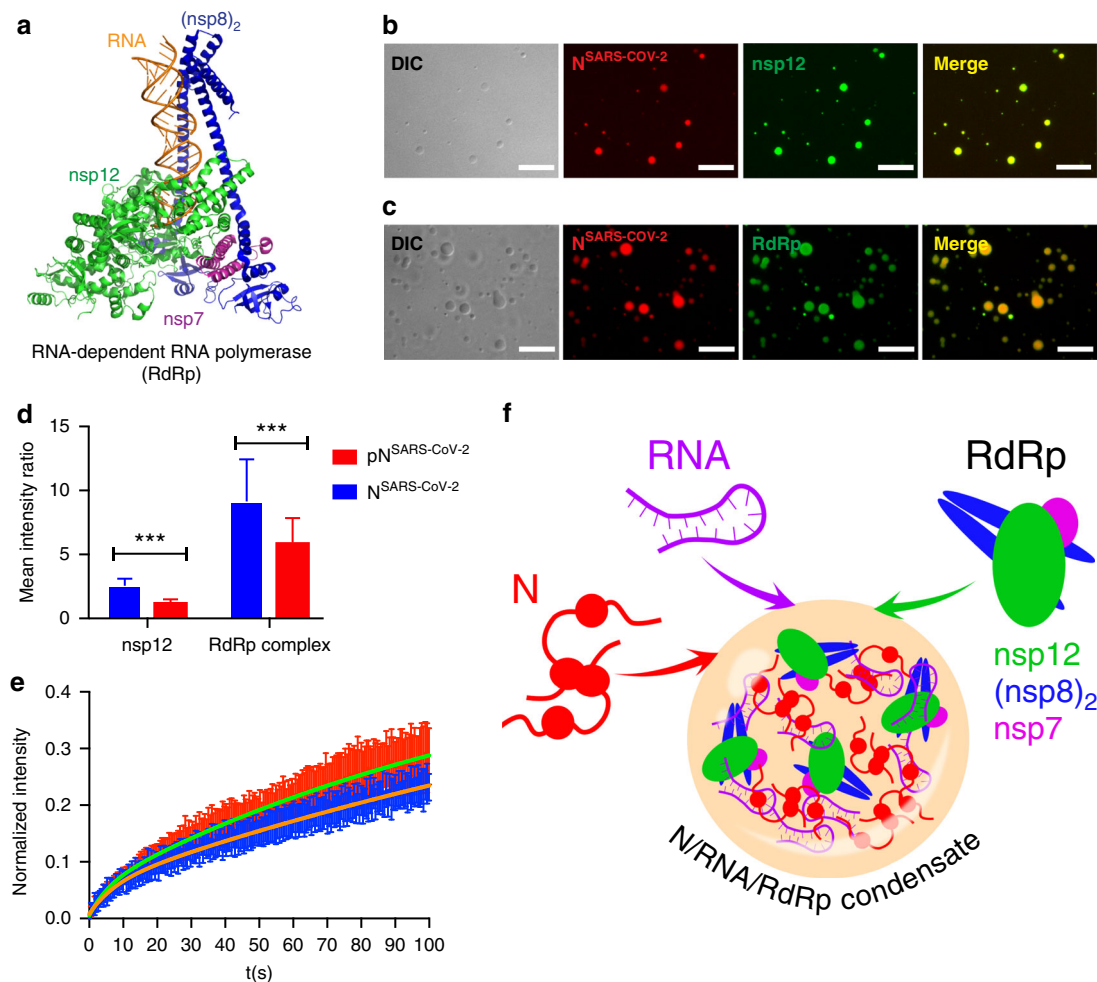


Fig. 5 The RNA-dependent RNA polymerase complex of SARS-CoV-2 concentrates in RNA/nucleocapsid protein-droplets. **a** Structure of the RNA-bound RdRp-complex formed by the SARS-CoV-2 non-structural proteins nsp12 (green), nsp7 (magenta) and nsp8 (blue) in 1:1:2 stoichiometry (PDB code: 6YYT)²⁹. **b** Fluorescence and DIC microscopy show the recruitment of Alexa Fluor 488 labeled nsp12 (green), the catalytic subunit of the RdRp-complex, into $N^{\text{SARS-CoV-2}}$ /polyU droplets ($N^{\text{SARS-CoV-2}}$ in red). **c** Active SARS-CoV-2 RdRp-complex bound to a fluorescein-labeled minimal RNA hairpin concentrates inside of $N^{\text{SARS-CoV-2}}$ /polyU droplets. In **(b)** and **(c)** droplets of $50 \mu\text{M}$ $N^{\text{SARS-CoV-2}}$ and $1 \mu\text{M}$ polyU were prepared in 20 mM NaPi, pH 7.5, and visualized by the addition of a small amount of Alexa Fluor 594 labeled $N^{\text{SARS-CoV-2}}$ protein. Scale bars are $10 \mu\text{m}$ in **(b)** and **(c)**. Micrographs are representative of three independent biological replicates. **d** Recruitment of nsp12 and RdRp complex into polyU-induced droplets of unmodified (blue) and SRPK1-phosphorylated (red) $N^{\text{SARS-CoV-2}}$. Mean values and standard deviation are shown ($n = 100$ droplets). Two-sided t-test with P value set to < 0.05 for statistical significance, $*** < 0.001$, $** < 0.002$ and $* < 0.033$, $ns < 0.12$. **e** FRAP of nsp12 after recruitment into $N^{\text{SARS-CoV-2}}$ /polyU (blue) and SRPK1-phosphorylated $N^{\text{SARS-CoV-2}}$ /polyU (red) droplets. Error bars represent the standard deviation for averaged 10 and 11 curves for unmodified and phosphorylated $N^{\text{SARS-CoV-2}}$, respectively. **f** Schematic representation of the LLPS-based formation of N/RNA/RdRp-condensates as protein/RNA-dense sites for viral transcription.

LLPS-based mechanisms similar to transcription hubs in cellular nuclei^{32,33} to enable high initiation and elongation rates during viral transcription. Because the replication machinery of coronaviruses is membrane-associated³⁴, it will furthermore be interesting to investigate if the SARS-CoV-2 glycoprotein M, which binds nucleocapsid protein⁴, causes tethering of $N^{\text{SARS-CoV-2}}$ /RdRp/RNA-condensates to host cell membranes.

Taken together the data suggest that inhibition of the RNA-induced phase separation of the nucleocapsid protein of SARS-CoV-2 provides a viable and novel strategy for the design of therapeutics to treat Covid-19.

Methods

Materials. Alexa Fluor 594 conjugated anti G3BP1 antibody was purchased from Santa Cruz Biotechnology (sc-365338 AF594). Digitonin was from Merck (CAS 11024-24-1). PolyU potassium salt (800 kDa) was purchased from Sigma-Aldrich (CAS Number 27416-86-0). Recombinant nucleocapsid protein of SARS-CoV-2 (Catalog No: Z03488-1) and SRPK1 kinase (Catalog No: PV4215) were purchased

from GenScript and ThermoFisher, respectively. The SR peptide, comprising residues 182-197 of the nucleocapsid protein of SARS-CoV-2, was produced by Fmoc-solid-phase synthesis using an automated microwave peptide synthesizer (Liberty 1, CEM) with acetyl- and amide protection groups at the N- and C-termini, respectively, and further purified by reverse-phase high-performance liquid chromatography (LC). Peptide masses were determined by LC-MS using an Acquity Arc System (WATERS) with SQD2-mass-detector.

Purification of nsp12, nsp7, nsp8 and formation of RdRp complex. Nsp12, nsp7, and nsp8 were expressed and purified as previously described²⁹. nsp12 was expressed in Hi5 insect cells using the pFastBac-His-MBP-SCoV2-nsp12 plasmid (Addgene #154759). Cells were collected by centrifugation, resuspended in lysis buffer (300 mM NaCl, 50 mM Na-HEPES pH 7.4, 10% (v/v) glycerol, 30 mM imidazole pH 8.0, 5 mM β -mercaptoethanol, $0.284 \mu\text{g ml}^{-1}$ leupeptin, $1.37 \mu\text{g ml}^{-1}$ pepstatin, 0.17 mg ml^{-1} PMSF and 0.33 mg ml^{-1} benzamidine, 3 mM MgCl_2) and immediately sonicated. Lysates were cleared by centrifugation, filtered ($0.8 \mu\text{m}$), and applied to a HisTrap HP 5 ml (GE Healthcare) preequilibrated in lysis buffer. The protein was eluted from the HisTrap column directly onto an XK column 16/20 (GE Healthcare), prepacked with amylose resin (New England Biolabs), using nickel elution buffer (300 mM NaCl, 50 mM Na-HEPES pH 7.4, 10% (v/v) glycerol,

500 mM imidazole pH 8.0, 3 mM MgCl₂ and 5 mM β-mercaptoethanol). Protein was eluted from the amylose column using amylose elution buffer (300 mM NaCl, 50 mM Na-HEPES pH 7.4, 10% (v/v) glycerol, 116.9 mM maltose, 30 mM imidazole pH 8.0 and 5 mM β-mercaptoethanol). Peak fractions containing nsp12 were pooled, cleaved with His-tagged TEV (12 h), and applied to a HisTrap column to remove uncleaved nsp12, 6×His-MBP, and TEV. The flow-through containing nsp12 was applied to a HiTrap Heparin 5 ml column (GE Healthcare). The flow-through containing nsp12 was collected, concentrated, and applied to a HiLoad S200 16/600 pg equilibrated in the size-exclusion buffer (300 mM NaCl, 20 mM Na-HEPES pH 7.4, 10% (v/v) glycerol, 1 mM MgCl₂, 1 mM TCEP). Peak fractions were pooled, concentrated until 102 μM, aliquoted, flash-frozen, and stored at -80 °C until use.

Nsp7 and nsp8 were expressed in E.coli using the pET-His-SCoV2-nsp7 plasmid (Addgene #154757) and pET-His-CoV2-nsp8 plasmid (Addgene #154758), respectively. Proteins were overexpressed in E. coli BL21 (DE3) RIL cells, grown in LB medium, collected by centrifugation, resuspended in lysis buffer (300 mM NaCl, 50 mM Na-HEPES pH 7.4, 10% (v/v) glycerol, 30 mM imidazole pH 8.0, 5 mM β-mercaptoethanol, 0.284 μg ml⁻¹ leupeptin, 1.37 μg ml⁻¹ pepstatin, 0.17 mg ml⁻¹ PMSF and 0.33 mg ml⁻¹ benzamide) and immediately sonicated. Both nsp8 and nsp7 were purified separately using the same purification procedure. Lysates were cleared by centrifugation and the supernatants applied to a HisTrap HP 5 ml column (GE Healthcare) pre-equilibrated in lysis buffer. The sample was eluted using nickel elution buffer (150 mM NaCl, 50 mM Na-HEPES pH 7.4, 10% (v/v) glycerol, 500 mM imidazole pH 8.0, and 5 mM β-mercaptoethanol) and the eluted protein dialyzed in dialysis buffer (150 mM NaCl, 50 mM Na-HEPES pH 7.4, 10% (v/v) glycerol and 5 mM β-mercaptoethanol) in the presence of His-tagged TEV (12 h at 4 °C). After adding imidazole pH 8.0, the sample was applied to a HisTrap HP 5 ml column (GE Healthcare). The flow-through with the protein of interest was then applied to a HiTrap Q 5 ml column (GE Healthcare) and the concentrated new flow-through applied to a HiLoad S200 16/600 pg equilibrated in size exclusion buffer (150 mM NaCl, 20 mM Na-HEPES pH 7.4, 5% (v/v) glycerol, 1 mM TCEP). Peak fractions were pooled, concentrated, aliquoted, flash-frozen, and stored at -80 °C until use. Protein purifications were performed at 4 °C.

For the preparation of the fluorescently labeled RNA, an RNA scaffold for RdRp/RNA complex formation was annealed by mixing equimolar amounts of two RNA strands (5'-rUrUrUrCrArUrGrCrArUrCrGrCrGrArG rGrCrUrCrArUrArCrCrGrUrArUrUrGrArGrA -3'; 56-FAM/rUrCrUrCrArArUrArCrGrGrUrArUrUrGrArGrC CrUrArCrGrCrG-3') (IDT Technologies) in annealing buffer (10 mM Na-HEPES pH 7.4, 50 mM NaCl) and heating to 75 °C, followed by step-wise cooling to 4 °C. For complex formation, 2.45 nmol of purified nsp12 was mixed with a 1.1-fold molar excess of RNA scaffold and 3-fold molar excess of each nsp8 and nsp7. After incubation at room temperature for 10 min, the complex was subjected to size exclusion chromatography on a Superdex 200 Increase 3.2/300 equilibrated with complex buffer (20 mM Na-HEPES pH 7.4, 100 mM NaCl, 1 mM MgCl₂, 1 mM TCEP). Peak fractions with a volume of approx. 125 μL (absorbance at 280 nm of 2.7 AU, 10 mm path length) corresponding to a nucleic acid-rich high-molecular-weight population (as judged by absorbance at 260 nm) were pooled and used for subsequent experiments.

Turbidity measurements. Phase diagrams of non-phosphorylated and phosphorylated N^{SARS-CoV-2} at different concentrations were determined using a NanoDrop spectrophotometer (ThermoFisher Scientific, Invitrogen). Increasing concentrations of polyU (0–2 μM) were added immediately before the experiments, followed by thoroughly pipetting and measurement of turbidity at 350 nm UV-Vis. Averages turbidity values were derived from measurements of three independent, freshly prepared samples.

Microscopy. For fluorescence microscopy, proteins were labeled using Alexa-fluor 488TM (green) or Alexa-fluor 594TM (red) microscale protein labeling kits (ThermoFisher Scientific, Invitrogen). Small amounts (~0.3 μl) of fluorescently-labeled N^{SARS-CoV-2} were premixed with unlabeled N^{SARS-CoV-2} and diluted to 50 μM final concentration with NaPi 20 mM buffer, pH 7.5. PolyU was added to the mixture to reach a final concentration of 1 μM. A total of 5 μl of the sample was subsequently loaded onto a slide and covered with a 18 mm coverslip. DIC and fluorescent micrographs were acquired on a Leica DM6B microscope with a 63x objective (water immersion) and processed using Fiji software (NIH). For RNA recruitment assays, fluorescently labeled RNA was premixed with 1 μM polyU and subsequently added to the mixture of fluorescently labeled/unlabeled N^{SARS-CoV-2}. For nsp12/RdRp/RNA recruitment assays, the fluorescently labeled component (FAM-labeled RNA scaffold, nsp12, or RdRp/RNA-complex) was premixed with 1 μM polyU, followed by addition to a mixture of fluorescently labeled/unlabeled N^{SARS-CoV-2}.

Quantification of the recruitment of fluorescently labeled RNA, nsp12, and RdRp complex into unmodified and SRPK1-phosphorylated N^{SARS-CoV-2}. The partition coefficient of either fluorescently labeled RNA, nsp12 or the RdRp complex was calculated from microscopy data using the Fiji software. For each of

the above-mentioned conditions, the partition coefficient was calculated as,

$$\text{Partition coefficient} = \frac{\text{Fluorescence Mean intensity}}{\text{Background Mean intensity}} \quad (1)$$

where the fluorescence mean intensity is the averaged droplet intensity calculated by defining its area and the background mean intensity corresponds to the averaged intensity of the background. For quantification of the partition coefficient of fluorescently labeled RNA, nsp12, or the RdRp complex, two independent samples were used and a total amount of 100 droplets per condition were analyzed. A two-tailed t-test was used to compare the partition coefficient values obtained for either fluorescently labeled RNA, nsp12, or the RdRp complex recruited into N^{SARS-CoV-2} (used as a control group) and phosphorylated N^{SARS-CoV-2}. A P value < 0.05 was set for statistical significance. The t-test was performed in Graph Prism.

Fluorescence recovery after photobleaching (FRAP). Dynamics of N^{SARS-CoV-2} molecules in the phase-separated state were investigated by FRAP analysis. As described above, N^{SARS-CoV-2} phase separation was induced using 50 μM N^{SARS-CoV-2} and 1 μM polyU in 20 mM sodium phosphate buffer (NaPi), pH 7.5. For comparison of the kinetics of unmodified and SRPK1 phosphorylated N^{SARS-CoV-2} protein, droplets of 30 μM nucleocapsid protein induced by the addition of 0.4 μM polyU were used. Droplet movement was reduced through the addition of 5% dextran T500 (Pharmacosmos). The sample was spiked with a small amount of Alexa Fluor 488 lysine labeled unmodified or SRPK1 phosphorylated N^{SARS-CoV-2}, or labeled nsp12 in the case of investigating the kinetics of nsp12 in droplets of unmodified or SRPK1 phosphorylated N^{SARS-CoV-2} (30 μM nucleocapsid protein, 0.3 μM polyU in 20 mM sodium phosphate buffer (NaPi), pH 7.5.). Labeled proteins were photobleached and followed during recovery. FRAP recordings were done on freshly formed droplets settled down on the glass slide (early time points; time of recording <15 min) and after one hour of sample incubation on the glass (late time points). For FRAPs of unmodified and SRPK1 phosphorylated N^{SARS-CoV-2} recordings were done in late time points.

FRAP experiments were recorded on a Leica TCS SP8 confocal microscope using a 63x objective (oil immersion) and a 488 argon laser line. A circular region of ~4 μm in diameter was chosen in a region of homogenous fluorescence away from the droplet boundary and bleached with five iterations of full laser power. Recovery was imaged at low laser intensity (5%). 100 frames were recorded with one frame per 523 ms. Pictures were analyzed in FIJI software (NIH) and FRAP recovery curves were calculated using standard methods on the basis of fluorescence intensities measured for prebleaching, bleached, and reference ROI. The prebleaching ROI was a selected region in the droplet before bleaching; the bleached ROI corresponded to the bleached area while the reference ROI corresponded to an area that did not experience bleaching. The fluorescence intensity measured for each of the described ROIs was corrected by background subtraction: a region where no fluorescence was detected was used to calculate the background. Thus, the FRAP recovery was calculated as:

$$\text{FRAP} = \frac{I_{\text{Bleached}} - I_{\text{background}}}{I_{\text{Av.Prebleaching}}} \quad (2)$$

The value obtained was then corrected by multiplication with the acquisition bleaching correction factor (ABCF), which was calculated according to:

$$\text{ABCF} = \frac{I_{\text{reference}} - I_{\text{background}}}{I_{\text{Av.Reference}}} \quad (3)$$

Finally, the curves were normalized according to:

$$\text{Normalization} = \frac{I_{(t)} - \text{min.Intensity Value}}{1 - \text{min.Intensity Value}} \quad (4)$$

Values were averaged from six recordings for both early and late time points and the resulting FRAP curves ± standard deviation (std) were fitted for the early time points to a mono-exponential function:

$$y = a*(1 - \exp(-b*x)) + c \quad (5)$$

For the late time points, a bi-exponential function provided the best fitting:

$$y = a*(1 - \exp(-b*x)) + y + a2*(1 - \exp(-b2*x)) + c \quad (6)$$

The mobile and immobile fractions were calculated using the parameters a and c derived from each fitting, according to the following equations:

$$\text{Mobile fraction} = a + c \quad (7)$$

$$\text{Immobile fraction} = 1 - a - c \quad (8)$$

Stress granule co-localization and FRAP. HeLa cells (DSMZ-German Collection of Microorganisms and Cell Cultures GmbH, ACC 57) were grown in an incubator at 37 °C in a humidified atmosphere with 5% CO₂. One day before the stress granule co-localization assay and FRAP measurements cells were seeded in 96-well CELL-viewTM slides (Greiner Bio-One) with glass bottom suitable for imaging so that on the day of the measurement cells reached ~50% of confluence. Stress granule formation was induced by treatment with 0.5 mM sodium arsenite for 60 minutes. Subsequently, cell membranes were permeabilized by incubation in cell

permeabilization buffer (20 mM HEPES-KOH pH 7.5, 120 mM KOAc, 5 mM Mg(OAc)₂, 250 mM sucrose) supplemented with 60 µg/ml digitonin for 40 s. After washing cells four times with 100 µL of cell permeabilization buffer live recording was started on a Leica TCS SP8 confocal microscope using a 63x objective (oil immersion) and 488 argon laser or 561 laser lines. A mixture of 0.5 µm Alexa Fluor 488 lysine labeled N^{SARS-CoV-2} and 1:100 Alexa Fluor 594 conjugated G3BP1 antibody (Abcam, ab217225) in cell permeabilization buffer was added to the cells and movies were recorded with 512 × 512 pixel resolution at 1000 Hz speed and 1 s per frame for about 2–3 min. For FRAP measurements, individual stress granules were marked and photobleached with five iterations of full 488 argon laser power. Recovery was imaged at low laser intensity (8%). 200 frames were recorded with one frame per 523 ms. Pictures were analyzed in FIJI software (NIH) and FRAP recovery curves ± standard deviation were calculated and fitted using bi-exponential fit as described above. Non-bleached stress granules were used as a reference for calculations.

In vitro phosphorylation. Phosphorylation of a stock of 850 µM SR-peptide (1766.8 Da) was performed by incubation with 0.15 µM SRPK1 kinase at 23 °C overnight in a buffer containing 4 mM ATP, 5 mM MgCl₂, 1 mM DTT, and 5 mM EGTA. Because of the intrinsically disordered nature of the peptide, inactivation of the kinase was achieved by incubation of the sample at 65 °C for 20 min, followed by centrifugation at 15,000 × g for 30 min. Residual ATP, MgCl₂, and EGTA were removed by HPLC followed by mass spectrometry. Phosphorylation of 100 µM unlabeled N^{SARS-CoV-2} was performed by incubation with 0.5 µM of SRPK1 kinase. The reaction mixture was incubated at 23 °C overnight in a buffer containing 8 mM ATP, 5 mM MgCl₂, 1 mM DTT, and 5 mM of EGTA. Residual ATP, MgCl₂, and EGTA were removed by 4 times buffer exchange using a Vivaspin 500.5 molecular weight cut-off (Sartorius, Göttingen). Samples were loaded onto a SDS-PAGE gel to confirm phosphorylation.

Mutation frequency analysis. To examine the mutation frequency in SARS-CoV-2 sequences we used the database and resources from the China National Center for Bioinformatics, 2019 Novel Coronavirus Resource (<https://bigd.big.ac.cn/ncov?lang=en>; downloaded June 7, 2020, with 42,176 genome sequences). The mutations between the genome positions 28274 and 29530 were analyzed to get the mutation frequency for each codon.

NMR spectroscopy. One-dimensional (1D) ¹H NMR experiments and two-dimensional (2D) ¹H-¹H TOCSY, NOESY, and ¹H-¹⁵N/¹H-¹³C heteronuclear single quantum coherence (HSQC) experiments of the SR-peptide (residues A182-S197) of N^{SARS-CoV-2} were acquired at 5 °C on a Bruker 700 MHz spectrometer equipped with a triple-resonance 5 mm cryogenic probe using the software Top Spin 3.5 (Bruker). The peptide concentration was 4 mM for resonance assignment and 200 µM for the interaction analysis with polyU (800 kDa). Samples were in 50 mM NaP, 0.01% NaN₃ and 5% D₂O. Spectra were processed with TopSpin 3.6 (Bruker) and analyzed using Sparky³⁵. Secondary structure was analyzed subjecting experimental HA, HN, N, CA and CB chemical shifts to TALOS+³⁶. The chemical shift perturbation (CSP) for the peptide residues is the one of the NH protons from the TOCSY experiment. The CSP error is based on the resolution of the spectra.

Molecular dynamics simulations. Starting structures of the SR-peptides were built in the PyMOL Molecular Graphics System (Version 1.8.4.0, Schrödinger, LLC), those of the RNA molecules using the RNA modeling software SimRNA³⁷. Initially, the different mixtures were equilibrated with 50,000 steps of energy minimization. To further equilibrate the system, 100 ps each of volume (NVT) and pressure (NPT) equilibration were performed without position restraints in order to have different starting points in each simulation. The MD simulations were carried out in GROMACS (version 2018.3) using the AMBER99SB-ILDN force field and the TIP3P water model at a temperature of 300 K, 1 bar of pressure and with a coupling time (τ_T) of 0.1 ps. The mixtures were solvated in water with 150 mM NaCl, ensuring overall charge neutrality. The particle mesh Ewald algorithm was used for calculation of the electrostatic term, with a radius of 16 Å for the grid-spacing and Fast Fourier Transform. The cut-off algorithm was applied for the non-coulombic potential with a radius of 10 Å. The LINCS algorithm was used to contain bonds and angles. MD simulations were performed during 1 or 100 ns in 2 fs steps and saving the coordinates of the system every 10 ps. The force field parameters for the phosphorylated amino acids were taken from³⁸. The number of contacts and secondary structure over the simulation trajectory were analyzed using the PyMOL Molecular Graphics System (Version 1.8.4.0, Schrödinger, LLC). To get error bars, 5 repetitions were done for each 1 ns simulation. For 100 ns simulations the error is the standard deviation over the trajectory.

Reporting summary. Further information on experimental design is available in the Nature Research Reporting Summary linked to this paper.

Data availability

NMR assignments are available in the BMRB (code 50379). The mutation frequency from SARS-CoV-2 sequences were obtained from the database and resources of the

China National Center for Bioinformatics, 2019 Novel Coronavirus Resource (<https://bigd.big.ac.cn/ncov?lang=en>; downloaded June 7, 2020, with 42,176 genome sequences). Authors can confirm that the rest of the relevant data are included in the paper and/or its supplementary information files. Other data that support the findings of this study are available from the corresponding author upon reasonable request. Source data are provided with this paper.

Received: 5 August 2020; Accepted: 29 October 2020;
Published online: 27 November 2020

References

- Zhou, P. et al. A pneumonia outbreak associated with a new coronavirus of probable bat origin. *Nature* **579**, 270–273 (2020).
- Virological.org. Novel 2019 Coronavirus Genome. Available online: <http://virological.org/t/novel-2019-coronavirus-genome/319>. (2020).
- Watanabe, Y., Allen, J. D., Wrapp, D., McLellan, J. S. & Crispin, M. Site-specific glycan analysis of the SARS-CoV-2 spike. *Science* **369**, 330–333 (2020).
- McBride, R., van Zyl, M. & Fielding, B. C. The coronavirus nucleocapsid is a multifunctional protein. *Viruses* **6**, 2991–3018 (2014).
- Gralinski, L. E. & Menachery, V. D. Return of the Coronavirus: 2019-nCoV. *Viruses* **12**, 135 (2020).
- Liu, W. et al. Evaluation of nucleocapsid and spike protein-based ELISAs for detecting antibodies against SARS-CoV-2. *J. Clin. Microbiol.* **58**, e00461-20 (2020).
- Fehr, A. R. & Perlman, S. Coronaviruses: an overview of their replication and pathogenesis. *Methods Mol. Biol.* **1282**, 1–23 (2015).
- Lu, X. et al. US CDC Real-time reverse transcription PCR panel for detection of severe acute respiratory syndrome coronavirus 2. *Emerg. Infect. Dis.* **26**, 1654–1665 (2020).
- Burbelo, P. D. et al. Sensitivity in detection of antibodies to nucleocapsid and spike proteins of severe acute respiratory syndrome coronavirus 2 in patients with coronavirus disease 2019. *J. Infect. Dis.* **222**, 206–213 (2020).
- Alberti, S., Gladfelter, A. & Mittag, T. Considerations and Challenges in Studying Liquid-Liquid Phase Separation and Biomolecular Condensates. *Cell* **176**, 419–434 (2019).
- Forman-Kay, J. D., Kriwacki, R. W. & Seydoux, G. Phase Separation in Biology and Disease. *J. Mol. Biol.* **430**, 4603–4606 (2018).
- Novoa, R. R. et al. Virus factories: associations of cell organelles for viral replication and morphogenesis. *Biol. Cell* **97**, 147–172 (2005).
- Heinrich, B. S., Maliga, Z., Stein, D. A., Hyman, A. A. & Whelan, S. P. J. Phase transitions drive the formation of vesicular stomatitis virus replication compartments. *mBio*. **9**, e02290–17 (2018).
- Nikolic, J. et al. Negri bodies are viral factories with properties of liquid organelles. *Nat. Commun.* **8**, 58 (2017).
- Guseva, S. et al. Measles virus nucleocapsid and phosphoproteins form liquid-like phase-separated compartments that promote nucleocapsid assembly. *Sci. Adv.* **6**, eaaz7095 (2020).
- Ye, Q., West, A. M. V., Silletti, S. & Corbett, K. D. Architecture and self-assembly of the SARS-CoV-2 nucleocapsid protein. *bioRxiv* (2020).
- Maharana, S. et al. RNA buffers the phase separation behavior of prion-like RNA binding proteins. *Science* **360**, 918–921 (2018).
- Zhou, Y. & Routh, A. Mapping RNA-capsid interactions and RNA secondary structure within virus particles using next-generation sequencing. *Nucleic Acids Res.* **48**, e12 (2020).
- White, J. P. & Lloyd, R. E. Regulation of stress granules in virus systems. *Trends Microbiol.* **20**, 175–183 (2012).
- Eiermann, N., Haneke, K., Sun, Z., Stoecklin, G. & Ruggieri, A. Dance with the devil: stress granules and signaling in antiviral responses. *Viruses* **12**, 984 (2020).
- Gordon, D. E. et al. A SARS-CoV-2 protein interaction map reveals targets for drug repurposing. *Nature* **583**, 459–468. (2020).
- Hofweber, M. et al. Phase separation of FUS is suppressed by its nuclear import receptor and arginine methylation. *Cell* **173**, 706–719 (2018). e13.
- Jain, S. et al. ATPase-modulated stress granules contain a diverse proteome and substructure. *Cell* **164**, 487–498 (2016).
- Peng, T. Y., Lee, K. R. & Tarn, W. Y. Phosphorylation of the arginine/serine dipeptide-rich motif of the severe acute respiratory syndrome coronavirus nucleocapsid protein modulates its multimerization, translation inhibitory activity and cellular localization. *FEBS J.* **275**, 4152–4163 (2008).
- Wegener, M. & Muller-McNicoll, M. View from an mRNP: the roles of sr proteins in assembly, maturation and turnover. *Adv. Exp. Med. Biol.* **1203**, 83–112 (2019).

26. Pietrek, L. M., Stelzl, L. S. & Hummer, G. Hierarchical ensembles of intrinsically disordered proteins at atomic resolution in molecular dynamics simulations. *J. Chem. Theory Comput* **16**, 725–737 (2020).
27. Kwon, I. et al. Poly-dipeptides encoded by the C9orf72 repeats bind nucleoli, impede RNA biogenesis, and kill cells. *Science* **345**, 1139–1145 (2014).
28. Fukuhara, T. et al. Utilization of host SR protein kinases and RNA-splicing machinery during viral replication. *Proc. Natl Acad. Sci. USA* **103**, 11329–11333 (2006).
29. Hillen, H. S. et al. Structure of replicating SARS-CoV-2 polymerase. *Nature* **584**, 154–156 (2020).
30. Stertz, S. et al. The intracellular sites of early replication and budding of SARS-coronavirus. *Virology* **361**, 304–315 (2007).
31. Cascarina, S. M. & Ross, E. D. A proposed role for the SARS-CoV-2 nucleocapsid protein in the formation and regulation of biomolecular condensates. *FASEB J.* **34**, 9832–9842 (2020).
32. Boehning, M. et al. RNA polymerase II clustering through carboxy-terminal domain phase separation. *Nat. Struct. Mol. Biol.* **25**, 833–840 (2018).
33. Cramer, P. Organization and regulation of gene transcription. *Nature* **573**, 45–54 (2019).
34. Sola, I., Almazan, F., Zuniga, S. & Enjuanes, L. Continuous and discontinuous RNA synthesis in coronaviruses. *Annu Rev. Virol.* **2**, 265–288 (2015).
35. Lee, W., Tonelli, M. & Markley, J. L. NMRFAM-SPARKY: enhanced software for biomolecular NMR spectroscopy. *Bioinformatics* **31**, 1325–1327 (2015).
36. Shen, Y., Delaglio, F., Cornilescu, G. & Bax, A. TALOS+: a hybrid method for predicting protein backbone torsion angles from NMR chemical shifts. *J. Biomol. NMR* **44**, 213–223 (2009).
37. Magnus, M., Boniecki, M. J., Dawson, W. & Bujnicki, J. M. SimRNAweb: a web server for RNA 3D structure modeling with optional restraints. *Nucleic Acids Res.* **44**, W315–W319 (2016).
38. Craft, J. W. Jr. & Legge, G. B. An AMBER/DYANA/MOLMOL phosphorylated amino acid library set and incorporation into NMR structure calculations. *J. Biomol. NMR* **33**, 15–24 (2005).

Acknowledgements

We thank Hauke S. Hillen, Goran Kocic, Lucas Farnung and Patrick Cramer for preparation of nsp12 and the RdRp complex, and Kerstin Overkamp for peptide synthesis and mass spectrometry. M.Z. was supported by the Helmholtz society through the Impuls- und Vernetzungsfond 'Multiscale Bioimaging: From Molecular Machines to Networks of Excitable Cells', by the German Science Foundation through SPP2191 and by the advanced grant '787679 - LLPS-NMR' of the European Research Council.

Author contributions

A.S. conducted LLPS assays; A.I.d.O. performed bioinformatic analysis, NMR spectroscopy and MD simulations; M.R. performed FRAP and stress granule experiments; A.S., A.I.d.O., M.R. and M.Z. designed the project and wrote the paper.

Funding

Open Access funding enabled and organized by Projekt DEAL.

Competing interests

The authors declare no competing interests.

Additional information

Supplementary information is available for this paper at <https://doi.org/10.1038/s41467-020-19843-1>.

Correspondence and requests for materials should be addressed to M.Z.

Peer review information *Nature Communications* thanks the anonymous reviewer(s) for their contribution to the peer review of this work.

Reprints and permission information is available at <http://www.nature.com/reprints>

Publisher's note Springer Nature remains neutral with regard to jurisdictional claims in published maps and institutional affiliations.



Open Access This article is licensed under a Creative Commons Attribution 4.0 International License, which permits use, sharing, adaptation, distribution and reproduction in any medium or format, as long as you give appropriate credit to the original author(s) and the source, provide a link to the Creative Commons license, and indicate if changes were made. The images or other third party material in this article are included in the article's Creative Commons license, unless indicated otherwise in a credit line to the material. If material is not included in the article's Creative Commons license and your intended use is not permitted by statutory regulation or exceeds the permitted use, you will need to obtain permission directly from the copyright holder. To view a copy of this license, visit <http://creativecommons.org/licenses/by/4.0/>.

© The Author(s) 2020